

1
2 **Ratio Limits of Water Storage and Outflow in Rainfall-runoff Process**

3 **Yulong Zhu^a, Yang Zhou^b, Xiaorong Xu^c, Changqing Meng^d, and Yuankun Wang^{e*}**

4
5 **^aYulong Zhu**

6 School of Water Resources and Hydropower Engineering, North China Electric Power University,
7 Changping Beinong 2# 102206, Beijing, China. Email: zhuyulong@ncepu.edu.cn

8 **^bYang Zhou**

9 School of Water Resources and Hydropower Engineering, North China Electric Power University,
10 Changping Beinong 2# 102206, Beijing, China. Email: zhouyang@ncepu.edu.cn

11 **^cXiaorong Xu**

12 School of Water Resources and Hydropower Engineering, North China Electric Power University,
13 Changping Beinong 2# 102206, Beijing, China. Email: xxrong@ncepu.edu.cn

14 **^dChangqing Meng**

15 School of Water Resources and Hydropower Engineering, North China Electric Power University,
16 Changping Beinong 2# 102206, Beijing, China. Email: els_meng@ncepu.edu.cn

17 **^{e*}Yuankun Wang** (Corresponding author)

18 School of Water Resources and Hydropower Engineering, North China Electric Power University,
19 Changping Beinong 2# 102206, Beijing, China. Email: yuankunw@ncepu.edu.cn

21 **Abstract**

22 Flash floods typically occur suddenly within hours of heavy rainfall. Accurate forecasting of flash floods in
23 advance using the two-dimensional (2D) shallow water equations (SWEs) remains a challenge, due to the
24 governing equations of SWEs being difficult-to-solve partial differential equations (PDEs). Aiming at
25 shortening the computational time and gaining more time for issuing early warnings of flash floods, a new
26 relationship between water storage and outflow in the rainfall-runoff process is attempted to be constructed
27 by assuming the catchment as a water storage system. Through numerical simulations of the diffusion wave
28 (DW) approximation of SWEs, the water storage and discharge are found to be limited to envelope lines, and
29 the discharge/water depth process lines during water rising and falling showed a grid-shaped distribution.
30 Furthermore, if a catchment is regarded as a semi-open water storage system, there is a nonlinear relationship
31 between the inside average water depth and the outlet water depth, namely the water storage ratio curve,
32 which resembles the shape of a “plume”. In the case of an open channel without considering spatial
33 variability, the water storage ratio curve is limited to three values (i.e. the upper, the steady, and the lower
34 limit), which are found to be independent of meteorological (rainfall intensity), vegetation (Manning’s
35 coefficient), and terrain (slope gradient) conditions. Meteorological, vegetation, and terrain conditions only
36 affect the size of the “plume” without changing its shape. Rainfall, especially weak rain (i.e. when rainfall
37 intensity is less than 5.0 mm h^{-1}) significantly affects the fluctuations of the water storage ratio, which can be
38 divided into three modes, that is Mode I (inverse S-shape type) during the rainfall beginning stage, Mode II
39 (wave type) during the rainfall duration stage, and Mode III (checkmark type) during rainfall end stage.
40 Results indicate that the determination of the nonlinear relationship of the water storage ratio curve under
41 different geographical scenarios will provide new ideas for simulation and early warning of flash floods.

42

43 1. Introduction

44 Flood disaster is a significant global health and economic threat. Disastrous floods have caused millions
45 of fatalities in the twentieth century and billions of dollars in direct economic losses each year (Merkuryeva
46 et al., 2015; Merz et al., 2021; Ruidas et al., 2022). According to statistics (Lee et al., 2020), from 2001 to
47 2018, over 2,900 floods caused over 93,000 deaths and over 490 billion USD in economic damages
48 worldwide. Based on 250-meter resolution daily satellite images of 913 major flood events during the same
49 period, the total area inundated by floods is estimated to be 2.23 million km² and the directly affected
50 population is estimated to be 255 to 290 million (Tellman et al., 2021). With the influence of climate change
51 and extreme El Niño events (Ward et al., 2014; Cai et al., 2014), flood events caused by extreme
52 precipitation are occurring frequently in many regions around the world (Kirezci et al., 2020; Najibi and
53 Devineni, 2018; Almazroui, 2020). From 2020 to 2023, catastrophic floods caused by several extreme
54 rainfall events were reported in Germany (Tradowsky et al., 2023), China (Hsu et al., 2021), Italy (Valente et
55 al., 2023), Japan (Kobayashi et al., 2023), Pakistan (Nanditha et al., 2023) and other developed or developing
56 countries and regions, even in some desert areas, e.g. in the Taklimakan Desert and the Atacama Desert, as
57 reported by Li and Yao (2023) and by Cabré et al. (2023) respectively. Research show that under a high
58 emissions scenario, in latitudes above 40° north, compound flooding could become more than 2.5 times as
59 frequent by 2100 compared to the present (Bevacqua et al., 2020). It means that in the future, the fraction of
60 the global population at risk of floods will be growing.

61 Flood simulation provides an effective means of flood forecasting to reduce property and life losses in
62 flood-threatened areas around the world. Particularly, weather prediction-based distributed
63 hydrological/hydraulic models are considered to be an effective strategy for flood simulation (Ming et al.,
64 2020). Hence, a large number of scholars are committed to improving the simulation efficiency or simulation

65 accuracy of distributed hydrological/hydraulic models. Accordingly, they have developed many forms of
66 hydrological models and hydrodynamic models in the past decades. Among them, the hydrological models
67 include Stanford Watershed Model IV-SWM (Crawford and Linsley, 1966), SHE/MIKESHE model (Abbott
68 et al., 1986), Tank model (Sugawara, 1995), Soil and Water Assessment Tool-SWAT (Arnold and Williams,
69 1987), and TOPMODEL (Beven and Kirkby, 1979). The hydrodynamic models include the one-dimensional
70 (1D) Saint-Venant equation (Köhne et al., 2011), the two-dimensional (2D) SWEs (Camassa et al., 1994),
71 and the three-dimensional (3D) integrated equations of runoff and seepage (Mori et al., 2015). In addition, a
72 variety of hydrological-hydrodynamic coupling models have also been proposed by Kim et al. (2012), Liu et
73 al. (2019), Hoch et al. (2019), and other scholars. Particularly, SWEs are the main governing equations for
74 simulating floods. However, flood simulation based on SWEs is a time-consuming process due to its
75 governing equations being a hyperbolic system of first-order nonlinear partial differential equations (PDEs)
76 (Li and Fan, 2017). Therefore, many scholars attempted to improve the efficiency and accuracy of flood
77 simulation through computer technology e.g. applying GPU parallel computing (Crossley et al., 2010) or
78 advanced numerical scheme (Sanders et al., 2010). For hydrological studies, the performance of hydrological
79 modeling is usually challenged by model calibration and uncertainty analysis during modeling exercises (Wu
80 et al., 2021).

81 Efficient and stable solution of the hydrodynamic model has long been an important issue in flood
82 forecasting. Since the SWEs are nonlinear hyperbolic PDEs, the increase in the calculation domain and the
83 increase in the degree of discreteness will greatly increase the difficulty of solving SWEs. In addition, when
84 using high-resolution terrain to improve model calculation accuracy, non-physical phenomena such as false
85 high flow velocity in steep terrain will also occur, resulting in calculation distortion and a sharp increase in
86 calculation time. Hence, we try to ignore the complex exchange/transfer process of mass and momentum

87 (hydrodynamic models), and also abandon the empirical relationships (hydrological models) between the
 88 input (precipitation), the transmission (flow rate), and the output (discharge) in the catchment area. A
 89 catchment is regarded as a semi-open water storage system, and the complex problem is simplified into three
 90 megascopic variables, i.e. inflow, water storage, and outflow. For one watershed, the complex internal flow
 91 processes could be ignored if the physical mechanism between inflow, water storage, and outflow can be
 92 found under different meteorological, geographical, and geological conditions. In other words, if we can give
 93 a physical-based relationship between the three megascopic variables, flood forecasting will become much
 94 simpler.

95 2. Methods

96 An arbitrary catchment (Fig. 1b) could be assumed to be a conceptual water tank (Fig. 1a). In this water
 97 tank, according to the law of conservation of mass, the complex confluence process of surface runoff could
 98 be neglected and it can be described only by the relationship between input, storage and output, which can be
 99 expressed as Eq. 1,

$$100 \quad \underbrace{A \times \frac{dH}{dt}}_{\text{storage}} = \underbrace{R \times A}_{\text{rainfall}} - \underbrace{I \times A}_{\text{infiltration}} + \underbrace{F \times A}_{\text{exfiltration}} - \underbrace{E \times A}_{\text{evaporation}} - \underbrace{\frac{Q}{A} \times A}_{\text{discharge}} \quad (1)$$

101 where A is catchment area (m^2); t is time (s); H is internal average water depth (m); R is rainfall
 102 intensity (m s^{-1}); I is infiltration (m s^{-1}); F is exfiltration (m s^{-1}); E is evaporation (m s^{-1}) and Q is discharge
 103 ($\text{m}^3 \text{s}^{-1}$).

104 In this section, attentions are focused on the surface flow of runoff, so the runoff-atmosphere moisture
 105 exchange (evaporation) and runoff-soil moisture exchange (infiltration and/or exfiltration) are
 106 non-considered. Zhu et al. (2020) validated the effectiveness of a diffusion wave (DW) approximation of
 107 shallow water equations by numerical simulations for simulating ground surface runoff,

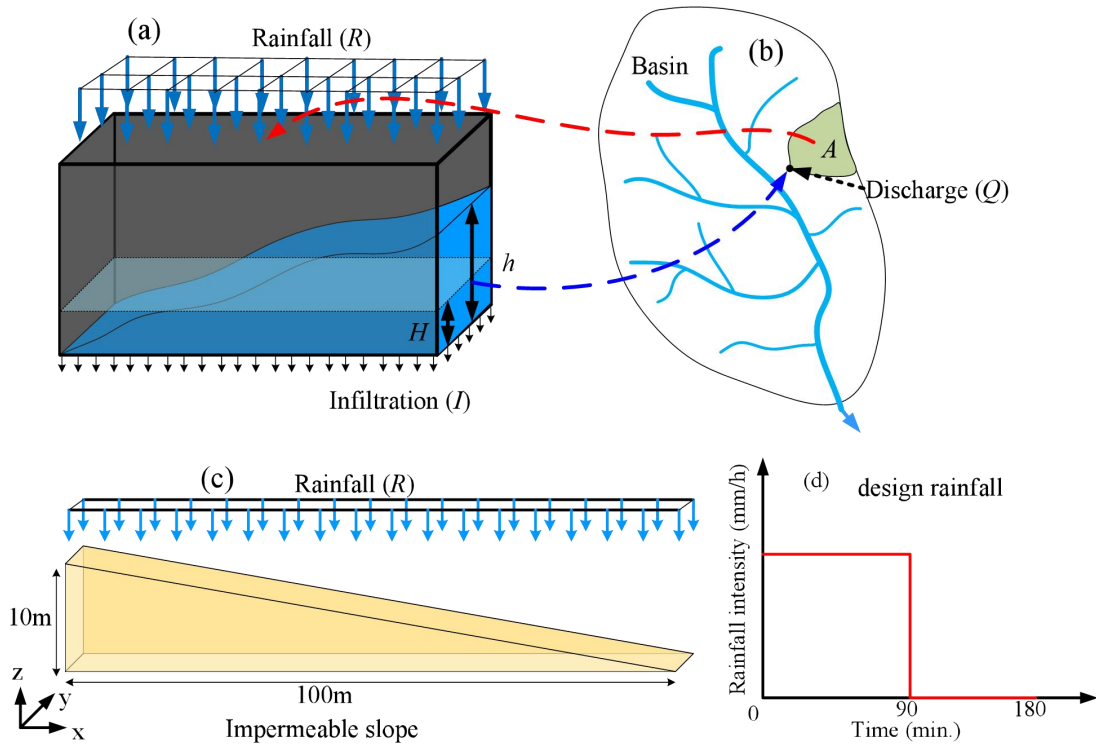
108
$$\frac{\partial h}{\partial t} - \nabla \left(\frac{h^{5/3}}{n_m \sqrt{|S|}} \nabla (h + z) \right) = R \quad (2)$$

109 where h is water depth (m); z is elevation (m); n_m is Manning's coefficient ($s \text{ m}^{-1/3}$) and S is the slope
 110 gradient.

111 To improve the computational efficiency of the hydrodynamic model, after strict mathematical
 112 derivation according to the basic hydrodynamic equation and the law of conservation of mass, Zhu et al.
 113 (2022) proposed a hydrological-hydrodynamic integrated model, i.e. distributed runoff model (DRM) as,

114
$$\begin{cases} \frac{dH}{dt} = R - q \\ H = \eta h = \eta \left(\frac{n_m}{\sqrt{S}} \right)^{0.6} q^{0.6} \left(\frac{A}{B} \right)^{0.6} \end{cases} \quad (3)$$

115 where $q=Q/A$ is conceptual outflow (m s^{-1}); η is the water storage ratio; B is the outlet width (m).

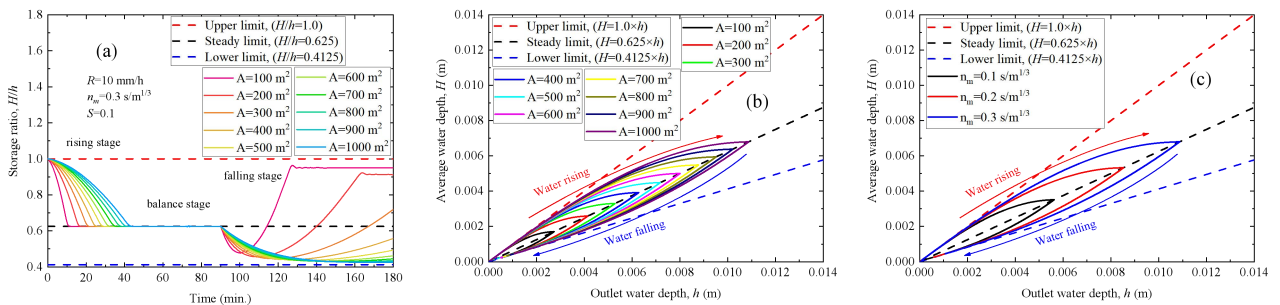


116
 117 **Fig. 1. Conceptual schematic of the DRM and numerical model.** (a) conceptual water tank; (b)
 118 conceptual catchment; (c) impermeable conceptual slope model; (d) design rainfall.

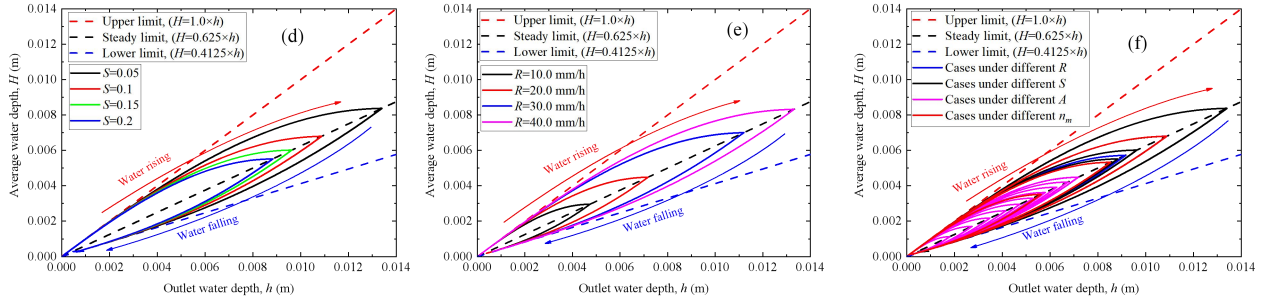
119 **3. Limits and “plume” shape of water storage ratio curve**

120 The conceptual hydrological model takes the inside average water depth (H) in the catchment area as

121 the independent variable (Eq. 1). However, the hydrodynamic equations take the water depth at any outlet (h)
 122 as an independent variable (Eq. 2). If a relationship between the inside average water depth (H) and outlet
 123 water depth (h) can be established, then this relationship will have both hydrodynamic and hydrological
 124 characteristics. Therefore, to find the H - h relationship, an impermeable conceptual slope model was built as
 125 shown in Fig. 1c, and numerical simulations were performed using diffusion wave (DW) approximation (Eq.
 126 2) of shallow water equations (SWEs). The water storage ratio is defined as the inside average water depth
 127 (H) divided by the outlet water depth (h). Firstly, the numerical simulations are performed under a designed
 128 rainfall condition, i.e. rainfall intensity is 10 mm h^{-1} and rainfall duration is 90 minutes with a total time of
 129 180 minutes as shown in Fig. 1d. From the time-dependent water storage ratio (H/h) under different
 130 catchment area (Fig. 2a), it can be seen that the continuous rainfall will cause the water storage ratio (H/h) to
 131 gradually decrease from the initial value 1.0 (upper limit) to a stable value, which is approximately 0.625
 132 (steady limit). When the rainfall ends, the value of the water storage ratio (H/h) decreases first and then
 133 increases, showing a U-shaped curve with a lower limit, which is approximately 0.4125. Afterward, the
 134 water storage ratio curves under ten kinds of catchment area (Fig. 2b), three kinds of Manning's coefficient
 135 (Fig. 2c), four kinds of slope gradient (Fig. 2d), and four kinds of rainfall intensity (Fig. 2e) conditions are
 136 obtained from parametric analyses and collected in Fig. 2f.



137



138

139 **Fig. 2. Water storage ratio curves.** (a) time-dependent water storage ratio under different catchment
 140 areas with 10 mm h^{-1} ; (b) water storage ratio curves under ten kinds of catchment area; (c) water storage ratio
 141 curves under three kinds of Manning's coefficient; (d) water storage ratio curves under four kinds of slope
 142 gradient; (e) water storage ratio curves under four kinds of rainfall intensity; (f) collection of the above
 143 twenty one water storage ratio curves. Three limit lines envelop all water storage ratio rising curves, i.e. upper limit
 144 ($H/h=1.0$), **steady limit** ($H/h=0.625$), and **lower limit** ($H/h=0.4125$).

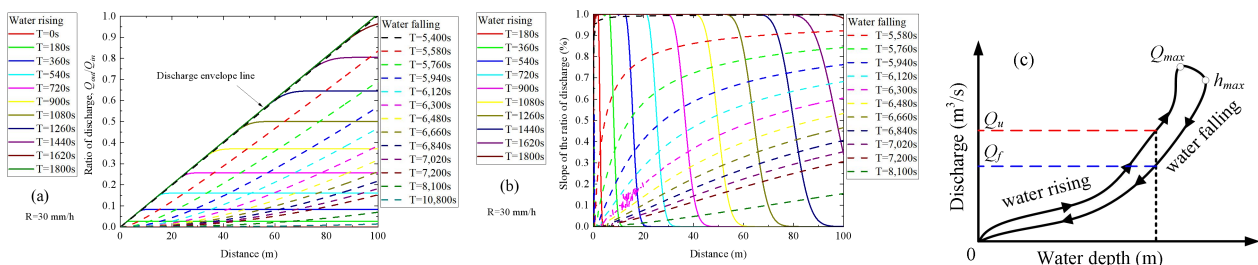
145 Finally, it is found that water storage ratio curves resemble the shape of a “plume”. When the water
 146 outlet depth is the same, the water storage ratio (H/h) of the water-rising limb is higher than that of the
 147 water-falling limb. Furthermore, in the case of an open channel without considering spatial variability, there
 148 are three limits (the upper, the steady, and the lower limit) of the water storage ratio curves, which are found
 149 to be independent of meteorological (rainfall intensity), vegetation (Manning's coefficient), and terrain (slope
 150 gradient) conditions. Meteorological, vegetation, and terrain conditions only affect the size of the “plume”
 151 without changing its shape which is anchored by three limits. This means that the three limits and the water
 152 storage ratio curves provide a key to establishing a relationship between the hydrodynamic models and the
 153 hydrological models.

154 **4. Grid-shaped cross-distribution of discharge/water depth process lines during water rising and**
 155 **falling**

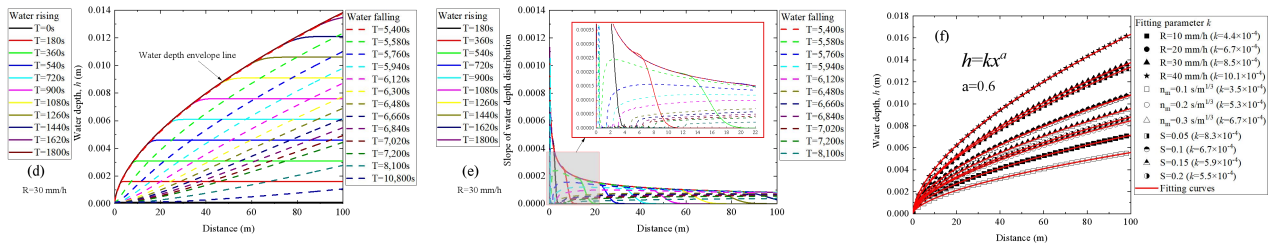
156 To obtain further insights into the causes for the formation of the water-rising limb and the water-falling

157 limb of the water storage ratio curve, the ratio of discharge (i.e. the ratio of the total outflows (Q_{out}) to the
 158 total inflows (Q_{in})), and the water depth (h) along the slope are discussed in Fig. 3a and Fig. 3d, respectively.
 159 Results indicate that there is an envelope line that controls the distribution of the discharge and water depth
 160 along the slope, respectively. The discharge envelope line is a straight line with a slope of 1% (Fig. 3a), while
 161 the water depth envelope line is a nonlinear curve controlled by a power function of general form $h=kx^a$ (Fig.
 162 3d). It means that if the duration of rainfall with a constant intensity is long enough, the catchment system
 163 will eventually reach an equilibrium state between inflow and outflow.

164 On the other hand, the process lines of discharge and water depth during water rising and falling present
 165 a grid-shaped cross-distribution (Fig. 3a and Fig. 3d). Similarly, from the view of the gradient of the
 166 discharge and water depth process lines during water rising and falling, the discharge gradient curves (Fig.
 167 3b) and the water depth gradient curves (Fig. 3e) also present a grid-shaped cross-distribution during water
 168 rising and falling, which might be the cause of the looped rating curve (Fig. 3c), i.e. higher discharges for the
 169 rising limb (Q_u) than for the recession limb (Q_f) at the same stage (Petersen-Overleir, 2006). After fitting the
 170 value of parameter k and a under different rainfall intensity (R), Manning's coefficient (n_m), and slope
 171 gradient (S) conditions (Fig. 3f), it is found that the parameter a is a constant, while the change of parameter
 172 k is positively correlated with the change of rainfall intensity (R) and Manning's coefficient (n_m), but
 173 negatively correlated with the change of slope gradient (S).



174



175

176

Fig. 3. Discharge/water depth process lines during water rising and falling. (a) discharge process lines

177

during water rising and falling; (b) gradient lines of discharge process line during water rising and falling; (c)

178

schematic diagram of looped rating curve; (d) water depth process lines during water rising and falling; (e)

179

gradient lines of water depth process lines during water rising and falling; (f) change of water depth envelope

180

line under different rainfall intensity (R), Manning's coefficient (n_m), and slope gradient (S).

181

Based on the water storage ratio curve, a hydrological-hydrodynamic integrated model, namely the

182

Distributed Runoff Model (DRM), is established with the governing equations in Eq. 3. To check the

183

effectiveness and applicability of DRM, a comparative analysis of the numerical results obtained from the

184

DRM and the DW model is implemented. We found that the DRM quickly reproduces the calculation results

185

of the time-consuming DW model under different rainfall intensities (Fig. 4a and Fig. 4b), different

186

Manning's coefficients (Fig. 4c), and different slope gradients (Fig. 4d). meaning that the water storage ratio

187

curve will provide new ideas for simulation and early warning of floods. In addition, due to the governing

188

equations of DRM being an ordinary differential equations (ODEs), the computational efficiency of DRM is

189

much higher than the DW model, which is governed by nonlinear partial differential equations (PDEs). More

190

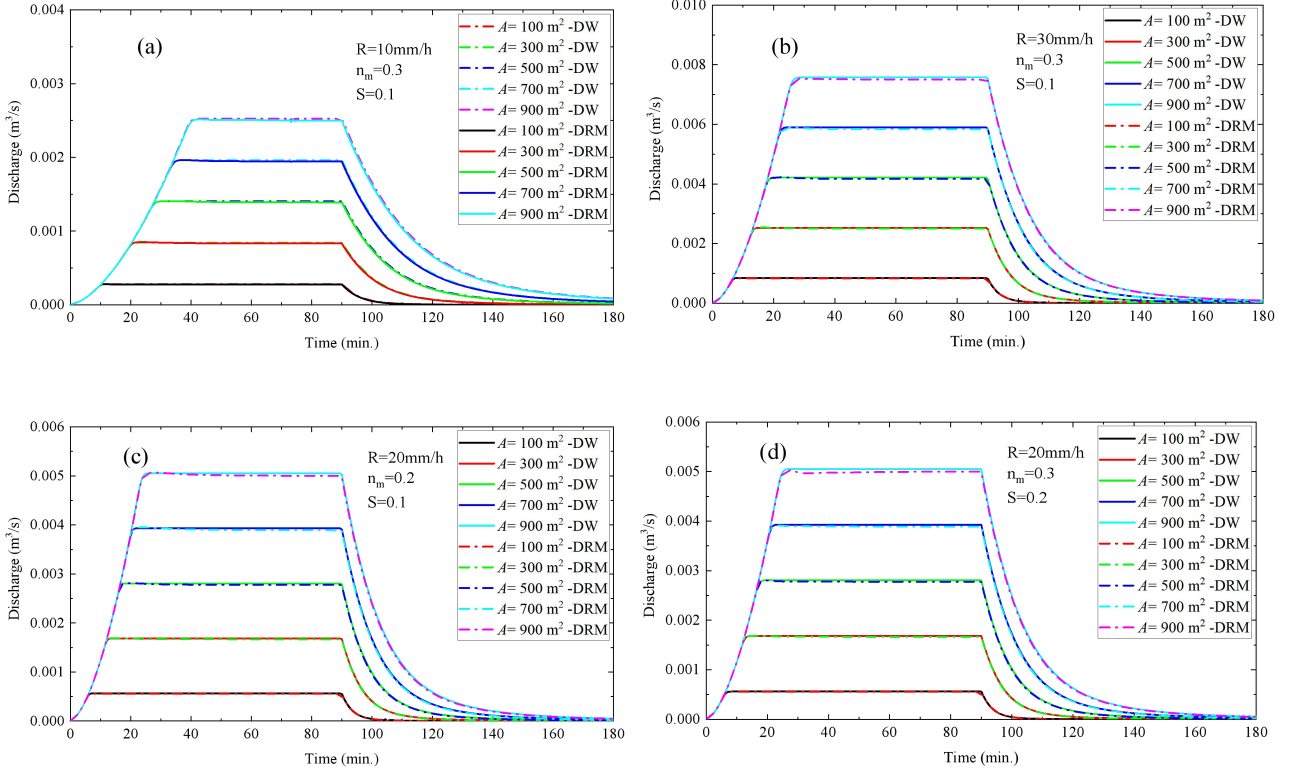
attention should be paid to the determination of the nonlinear relationship of the water storage ratio curve

191

under different geographical scenarios, which will be beneficial to the proposal of more efficient flood

192

forecasting methods or early warning systems.



193

194

195

196

197

198

199

200

201

202

203

204

205

Fig. 4. Comparative analyses of discharge calculated by DW and DRM under designed rainfall. (a) controlled group; (b) compared with (a), only the rainfall intensity is changed; (c) compared with (a), rainfall intensity and Manning coefficient are changed; (d) compared with (a), rainfall intensity and slope gradient are changed.

5. Validation of DRM by considering infiltration calculated by Horton infiltration method.

In the above section, the simulations of DW and DRM are based on an impermeable conceptual slope model as shown in Fig. 1c. After considering infiltration in the DW and DRM, Eq. 2 and Eq. 3 become:

$$\frac{\partial h}{\partial t} - \nabla \left(\frac{h^5}{n_m \sqrt{|S|}} \nabla (h + z) \right) = R - I \quad (4)$$

$$\begin{cases} \frac{dH}{dt} = R - q - I \\ H = \eta h = \eta \left(\frac{n_m}{\sqrt{S}} \right)^{0.6} q^{0.6} \left(\frac{A}{B} \right)^{0.6} \end{cases} \quad (5)$$

Infiltration (I) is calculated by Horton's infiltration model (Horton, 1933), which suggests an exponential equation for modeling the soil infiltration capacity f_p ($m s^{-1}$):

206
207

$$f_p(t) = f_c + (f_0 - f_c)e^{-kt} \quad (6)$$

208 where f_0 is the initial infiltration capacity (m s⁻¹), f_c is the final infiltration capacity (m s⁻¹), k represents
209 the rate of decrease in the capacity (s⁻¹). The infiltration parameter sets are listed in Table 1.

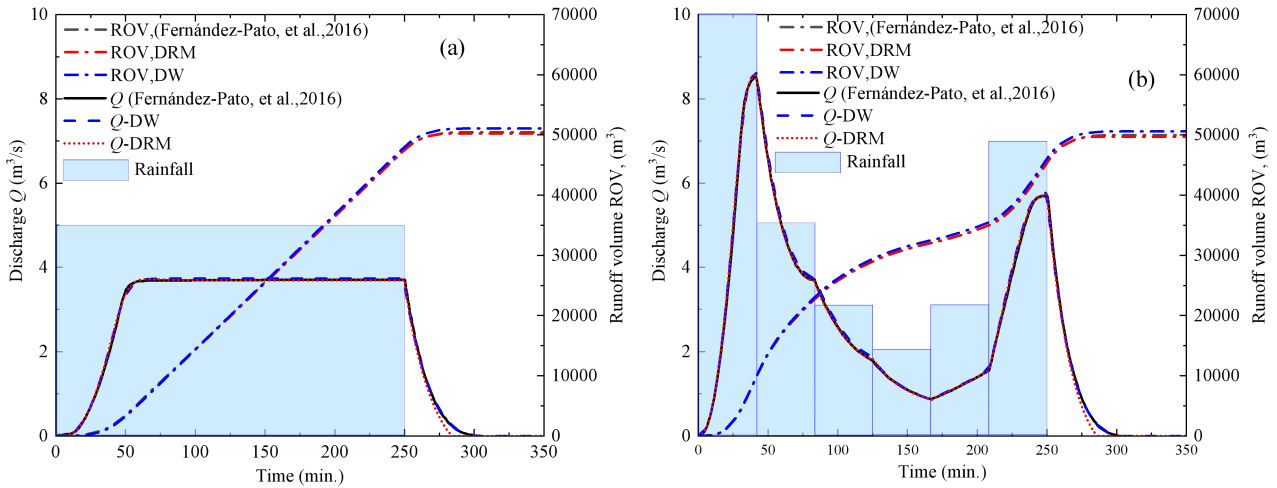
210 **Table 1** Infiltration parameter sets.

Parameter	k (s ⁻¹)	f_c (m s ⁻¹)	f_0 (m s ⁻¹)
Value	2.43×10 ⁻³	3.272×10 ⁻⁵	1.977×10 ⁻⁴

211 A rainfall event begins with a weak precipitation intensity. When the rainfall intensity is less than the
212 infiltration capacity, all the rainwater will infiltrate into the soil. While, when the rainfall intensity exceeds
213 the soil infiltration capacity, the surface water is generated, and Horton law (Eq. 6) applies:

$$I = \begin{cases} R(t) & \text{if } R(t) \leq f_p(t) \\ f_p(t) & \text{if } R(t) > f_p(t) \end{cases} \quad (7)$$

215 Results of outlet discharge (Q) and runoff volume (ROV) calculated by DW and DRM are compared
216 with the reference results adopted from Fernández-Pato et al. (2016) as shown in Fig. 5. Fig. 5a shows the
217 comparison of results under a uniform design rainfall. In this case, the rain volume is 75,000 m³ with a
218 duration of 250 minutes (min.). Fig. 5b shows the comparison of results under a non-uniform rainfall. Rain
219 volume is 75,000 m³ with a duration of 250 minutes (min.). From Fig. 5, it can be recognized that after
220 considering infiltration, except that the calculation results of DRM are a little small at the end-stage of
221 rainfall, the calculation results of DRM are still highly consistent with the calculation results of the DW
222 model and reference results adopted from Fernández-Pato et al. (2016).



223

224

Fig. 5. Outlet discharge (Q) and runoff volume (ROV) calculated by DW and DRM vs. reference

225

results adopted from Fernández-Pato et al. (2016).

226

6. Fluctuation of water storage ratio under natural rainfall conditions

227

After implementing a real rainfall event in the impermeable conceptual slope model (Fig. 1c), the

228

change of the water storage ratio is calculated as shown in Fig. 6. Rainfall data was recorded from 09 August

229

2022 00:00 to 10 August 2022 00:00 in Aomori Prefecture, Japan and from 29 August 2016 01:00 to 31

230

August 2016 09:00 in Nissho Pass, Japan (<https://www.data.jma.go.jp>). The total simulation time is 30 hours

231

and 56 hours, respectively. Results show that in addition to the fluctuations of water storage ratio in the

232

beginning and end stages of rainfall, there are mainly ten fluctuation periods of water storage ratio during the

233

rainfall duration stage, identified as 1[#], 2[#], 3[#], 4[#], and 5[#] in Fig. 6a and 6[#], 7[#], 8[#], 9[#], and 10[#] in Fig. 6b. The

234

fluctuations are found to be mainly caused by weak rainfall (i.e. rainfall intensity is near 5.0 mm h^{-1}) as

235

pointed by the red arrows in Fig. 6a and Fig. 6b. The magnitude of the fluctuations appears to be positively

236

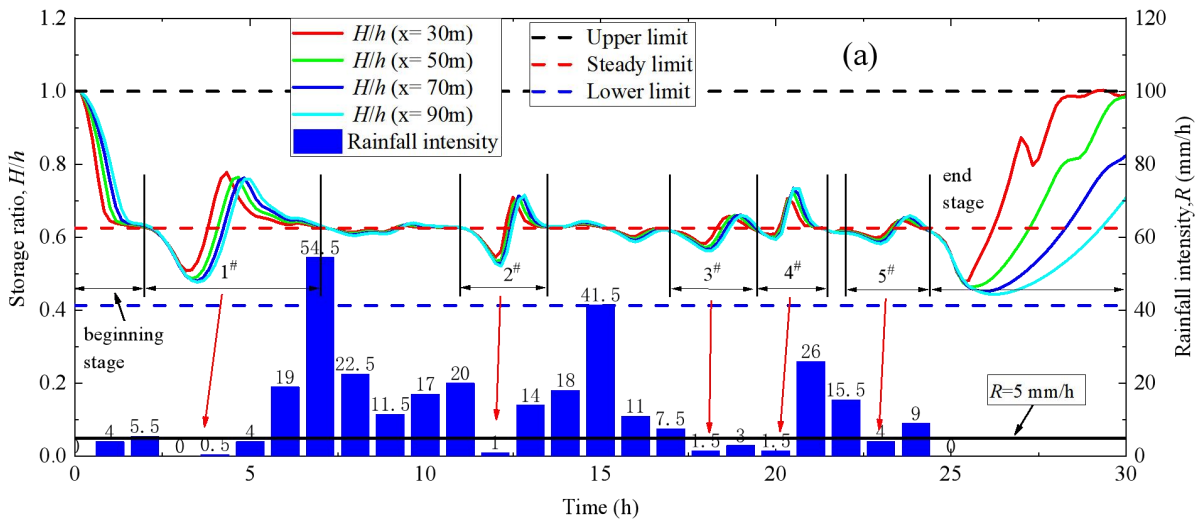
correlated with the difference between rainfall intensity and 5.0 mm h^{-1} . When the rainfall intensity continues

237

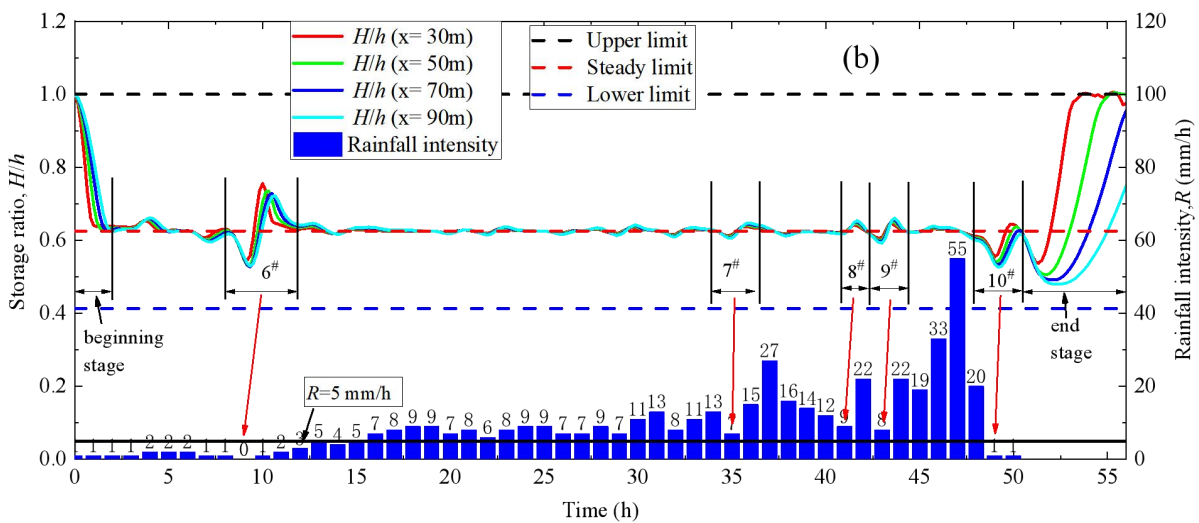
to be greater than 5.0 mm h^{-1} , the fluctuation of the water storage ratio is not obvious. The water storage ratio

238

is stable near the steady limit, even if there is heavy rainfall during this period.



239



240

241 **Fig. 6. The fluctuation of water storage ratio and the effectiveness of DRM in natural rainfall events. (a)**

242 **Aomori Prefecture; (b) Nissho Pass.**

243 Besides, the fluctuations of the water storage ratio can be divided into three modes, that is Mode I

244 identified as the inverse S-shape type during the rainfall beginning stage (Fig. 7a), Mode II identified as

245 wave type during the weak rainfall duration stage (Fig. 7b), and Mode III identified as checkmark type

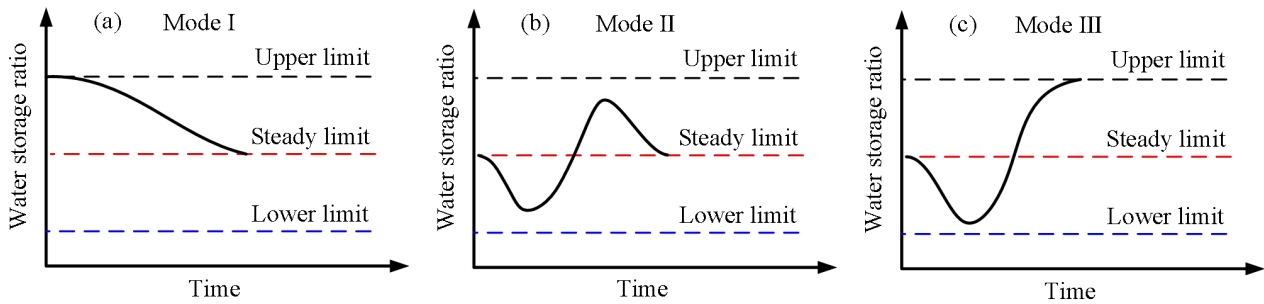
246 during rainfall end-stage (Fig. 7c). Among them, Mode I **describes how** water storage ratio drops from upper

247 limit to steady limit in an inverse S-shape. Mode II **represents the water storage fluctuations** around the

248 steady limit. Mode III **happens when** the water storage ratio first drops from the steady limit to the lower

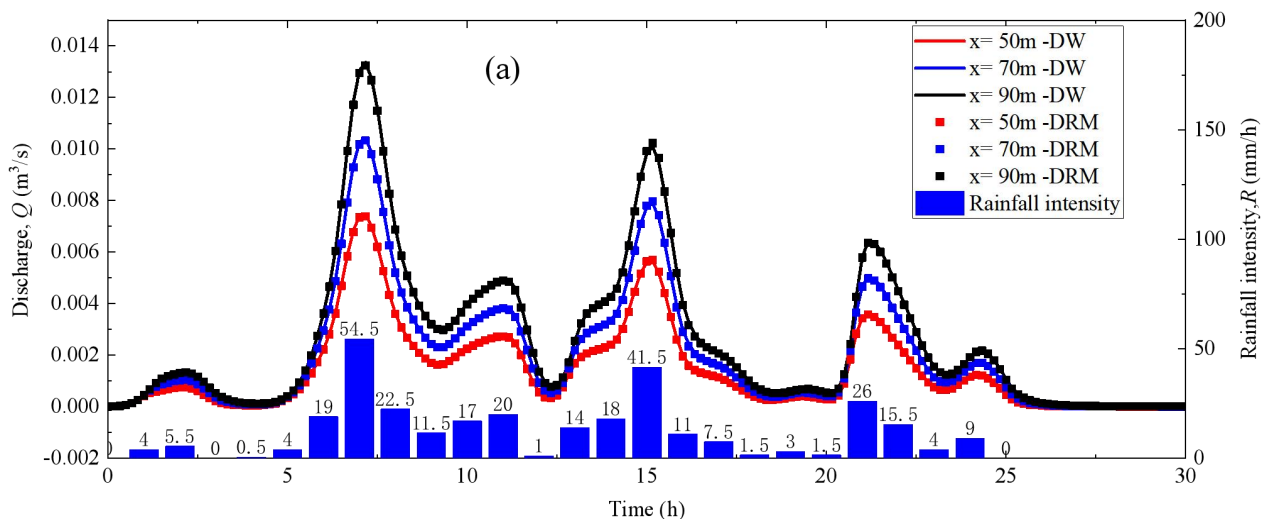
249 limit and then rises to the upper limit. This means that the certainty of the fluctuation modes will provide the

250 possibility for quantitative analysis of the fluctuation of the water storage ratio induced by the change in the
 251 rainfall intensity.

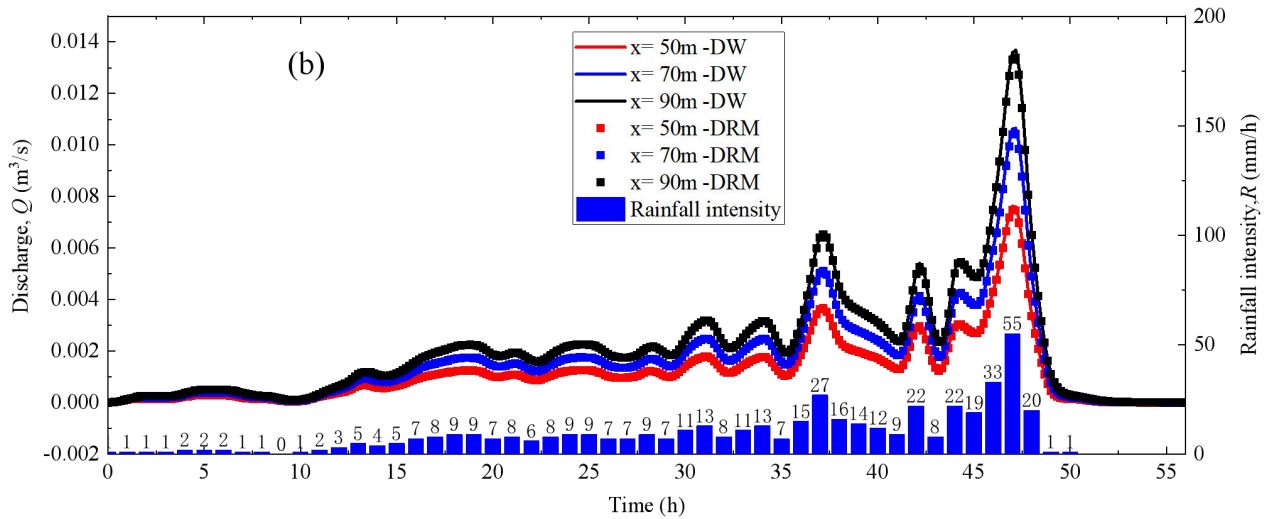


252
 253 **Fig. 7. Three kinds of water storage ratio fluctuation modes in natural rainfall events.** (a) Mode I during
 254 the rainfall beginning stage; (b) Mode II during the weak rainfall duration stage; (c) Mode III during the
 255 rainfall end stage.

256 Figures 8a and 8b show the simulation results of discharge calculated by the DRM and DW model using
 257 the rainfall data recorded in Aomori Prefecture and Nissho Pass, Japan, respectively. Results suggest that
 258 after the determination of the water storage ratio fluctuations, the calculation results of DRM are in good
 259 agreement with those of the DW model, meaning that DRM provides a new and more effective theoretical
 260 scheme for flood prediction.



261



262

263 **Fig. 8. Time-dependent discharge calculated by DRM and DW model. (a) Aomori Prefecture; (b) Nissho**

264

Pass.

265 **7. Discussions and Conclusions**

266 Based on a conceptual slope model, numerical simulations of the rainfall-runoff process are performed
 267 by using the diffusion wave (DW) approximation of SWEs. A “plume” shaped nonlinear relationship
 268 between water storage and outflow, defined as the water storage ratio, is found between the inside average
 269 water depth and the outlet water depth in a catchment. The water storage ratio is controlled by three limits,
 270 namely upper limit, steady limit, and lower limit with the value of approximately 1.0, 0.625, and 0.4125,
 271 respectively. Under the control of the three limits, meteorological, vegetation, and terrain conditions only
 272 affect the size of the “plume” without changing its shape. The regular curve shape of the water storage ratio
 273 provides the possibility to construct a correlation between the water storage in the catchment area and the
 274 outlet discharge.

275 Based on the water storage ratio, a hydrological-hydrodynamic integrated model (DRM), is established,
 276 which shows high calculation accuracy and computational efficiency. This is because the governing
 277 equations of DRM are ordinary differential equations (ODEs), which are much easier to solve than nonlinear

278 partial differential equations (PDEs). However, the calculations of DRM and DW only involve the
279 confluence part of surface water and infiltration, while the interbasin groundwater flow as inputs to the
280 watershed (exfiltration) and evaporation are not considered. This is inconsistent with the real rainfall-runoff
281 process in the watershed and may lead to deviations in the calculation results. Therefore, the flow exchange
282 between surface water and groundwater during the existence and extinction of runoff also needs to be further
283 realized by establishing a dynamic coupling model of surface water and groundwater.

284 In addition, the water storage and discharge are limited to envelope lines, and the discharge/water depth
285 process lines during water rising and falling showed a grid-shaped distribution, which might be the cause of
286 the looped rating curve, i.e. higher discharges for the rising limb than for the recession limb at the same stage.
287 Rainfall, especially weak rainfall (i.e. rainfall intensity less than 5.0 mm h^{-1}) significantly affects the
288 fluctuations of the water storage ratio. The fluctuations of water storage ratio during a real rainfall event can
289 be divided into three modes, that is Mode I identified as inverse S-shape type during the rainfall beginning
290 stage, Mode II identified as Wave type during weak rainfall duration stage, and Mode III identified as
291 checkmark type during rainfall end stage. It is worth noting that a qualitative determination of the three
292 fluctuation modes of water storage ratio during rainfall events is obtained, but the quantitative analysis still
293 needs to be further carried out in the future.

294 The findings in this study provide a key to establishing a simpler prediction model for flash floods. The
295 water storage ratio has been proven to be effective in improving the effectiveness and efficiency of flood
296 forecasting. Therefore, the determination of the nonlinear relationship of the water storage ratio curve under
297 different geographical scenarios will provide new ideas for simulation and early warning of flash floods.

298 **Authors' contributions**

299 **Yulong Zhu:** Conceptualization, Methodology, Software, Validation, Formal Analysis, Investigation, Data

300 Curation, Writing-Original draft, Writing - Review & Editing.

301 **Yang Zhou:** Methodology, Validation, Investigation, Resources, Data Curation.

302 **Xiaorong Xu:** Methodology, Investigation, Data Curation.

303 **Changqing Meng:** Validation, Investigation, Data Curation.

304 **Yuankun Wang:** Conceptualization, Methodology, Writing-Original draft, Writing - Review & Editing,

305 Supervision, Project administration, Funding acquisition.

306

307 **Availability of data and materials**

308 The datasets used and/or analyzed during the current study are available from the corresponding author on

309 reasonable request.

310

311 **Competing interests**

312 The authors declare that they have no conflict of interest.

313

314 **Acknowledgments**

315 This study was supported by the National Natural Science Fund of China (52279064, 52209087), and the

316 Fundamental Research Funds for the Central Universities of China (2024MS069, 2024MS068).

317

318 **References**

319 Abbott, M. B., Bathurst, J. C., Cunge, J. A., O'Connell, P. E., and Rasmussen, J.: An introduction to the

320 European Hydrological System-Systeme Hydrologique Europeen, "SHE", 1: History and philosophy of

321 a physically-based, distributed modelling system. *Journal of Hydrology*, 87(1-2), 45-59,

322 [https://doi.org/10.1016/0022-1694\(86\)90114-9](https://doi.org/10.1016/0022-1694(86)90114-9), 1986.

323 Almazroui, M.: Rainfall trends and extremes in Saudi Arabia in recent decades. *Atmosphere*, 11(9), 964,
324 <https://doi.org/10.3390/atmos11090964>, 2020.

325 Arnold, J. G., and Williams, J. R.: Validation of SWRRB: Simulator for water resources in rural basins. *J.*
326 *Water Resour. Plan. Manage.* ASCE, 113(2), 243-256,
327 [https://doi.org/10.1061/\(ASCE\)0733-9496\(1987\)113:2\(243\)](https://doi.org/10.1061/(ASCE)0733-9496(1987)113:2(243)), 1987.

328 Beven, K. J. and Kirkby, M. J.: A Physically Based Variable Contributing Area Model of Basin Hydrology.
329 *Hydrological Sciences Bulletin*, 24, 43-69, <https://doi.org/10.1080/02626667909491834>, 1979.

330 Bevacqua, E., Vousdoukas, M. I., Zappa, G., Hodges, K., Shepherd, T. G., Maraun, D., Mentaschi, L., and
331 Feyen, L.: More meteorological events that drive compound coastal flooding are projected under
332 climate change. *Communications Earth & Environment*, 1(1), 47,
333 <https://doi.org/10.1038/s43247-020-00044-z>, 2020.

334 Cabré, A., Remy, D., Marc, O., Burrows, K., and Carretier, S.: Flash floods triggered by the 15-17th March
335 2022 rainstorm event in the Atacama Desert mapped from InSAR coherence time series. *Natural*
336 *Hazards*, 116(1), 1345-1353, <https://doi.org/10.1007/s11069-022-05707-y>, 2023.

337 Cai, W., Borlace, S., Lengaigne, M., van Rensch, P., Collins, M., Vecchi, G., Timmermann, A., Santoso, A.,
338 McPhaden, M. J., Wu, L., England, M. H., Wang, G., Guilyardi, E., and Jin, F. F.: Increasing frequency
339 of extreme El Niño events due to greenhouse warming. *Nature Climate Change*, 4(2), 111-116,
340 <https://doi.org/10.1038/nclimate2100>, 2014.

341 Camassa, R., Holm, D. D., and Hyman, J. M.: A new integrable shallow water equation. *Advances in Applied*
342 *Mechanics*, 31, 1-33, [https://doi.org/10.1016/S0065-2156\(08\)70254-0](https://doi.org/10.1016/S0065-2156(08)70254-0), 1994.

343 Crawford, N. H. and Linsley, R. K.: Digital Simulation in Hydrology: Stanford Watershed Model IV.

344 Technical Report No. 39, Department of Civil Engineering, Stanford University, pp. 210, 1966.

345 Crossley, A., Lamb, R., Waller, S., and Dunning, P.: Fast 2D flood modelling using GPU technology-recent
346 applications and new developments. In EGU General Assembly Conference Abstracts, p. 12043, 2010.

347 Fernández-Pato, J., Caviedes-Voullième, D., and García-Navarro, P.: Rainfall/runoff simulation with 2D full
348 shallow water equations: Sensitivity analysis and calibration of infiltration parameters. *Journal of*
349 *hydrology*, 536, 496-513, <https://doi.org/10.1016/j.jhydrol.2016.03.021>, 2016.

350 Hoch, J. M., Eilander, D., Ikeuchi, H., Baart, F., and Winsemius, H. C.: Evaluating the impact of model
351 complexity on flood wave propagation and inundation extent with a hydrologic–hydrodynamic model
352 coupling framework. *Natural Hazards and Earth System Sciences*, 19(8), 1723-1735,
353 <https://doi.org/10.5194/nhess-19-1723-2019>, 2019.

354 Horton, R.: The role of infiltration in the hydrologic cycle. *Trans. Am. Geophys. Union* 14, 446-460,
355 <https://doi.org/10.1029/TR014i001p00446>, 1933.

356 Hsu, P. C., Xie, J., Lee, J. Y., Zhu, Z., Li, Y., Chen, B., and Zhang, S.: Multiscale interactions driving the
357 devastating floods in Henan Province, China during July 2021. *Weather and Climate Extremes*, 39,
358 100541, <https://doi.org/10.1016/j.wace.2022.100541>, 2023.

359 Kim, J., Warnock, A., Ivanov, V. Y., and Katopodes, N. D.: Coupled modeling of hydrologic and
360 hydrodynamic processes including overland and channel flow. *Advances in Water Resources*, 37,
361 104-126, <https://doi.org/10.1016/j.advwatres.2011.11.009>, 2012.

362 Kirezci, E., Young, I. R., Ranasinghe, R., Muis, S., Nicholls, R. J., Lincke, D., and Hinkel, J.: Projections of
363 global-scale extreme sea levels and resulting episodic coastal flooding over the 21st Century. *Scientific*
364 *Reports*, 10(1), 11629, <https://doi.org/10.1038/s41598-020-67736-6>, 2020.

365 Kobayashi, K., Duc, L., Kawabata, T., Tamura, A., Oizumi, T., Saito, K., Nohara, D., and Sumi, T.: Ensemble

366 rainfall–runoff and inundation simulations using 100 and 1000 member rainfalls by 4D LETKF on the
367 Kumagawa River flooding 2020. *Progress in Earth and Planetary Science*, 10(1), 1-22,
368 <https://doi.org/10.1186/s40645-023-00537-3>, 2023.

369 Köhne, J. M., Wöhling, T., Pot, V., Benoit, P., Leguédois, S., Le Bissonnais, Y., and Šimůnek, J.: Coupled
370 simulation of surface runoff and soil water flow using multi-objective parameter estimation. *Journal of*
371 *Hydrology*, 403(1-2), 141-156, <https://doi.org/10.1016/j.jhydrol.2011.04.001>, 2011.

372 Lee, J., Perera, D., Glickman, T., and Taing, L. Water-related disasters and their health impacts: A global
373 review. *Progress in Disaster Science*, 8, 100123, <https://doi.org/10.1016/j.pdisas.2020.100123>, 2020.

374 Li, M., and Yao, J.: Precipitation extremes observed over and around the Taklimakan Desert, China. *PeerJ*, 11,
375 e15256, <https://doi.org/10.7717/peerj.15256>, 2023.

376 Li, P. W., and Fan, C. M.: Generalized finite difference method for two-dimensional shallow water equations.
377 *Engineering Analysis with Boundary Elements*, 80, 58-71,
378 <https://doi.org/10.1016/j.enganabound.2017.03.012>, 2017.

379 Liu, Z., Zhang, H., and Liang, Q.: A coupled hydrological and hydrodynamic model for flood simulation.
380 *Hydrology Research*, 50(2), 589-606, <https://doi.org/10.2166/nh.2018.090>, 2019.

381 Merkuryeva, G., Merkuryev, Y., Sokolov, B. V., Potryasaev, S., Zelentsov, V. A., and Lektuers, A.:
382 Advanced river flood monitoring, modelling and forecasting. *Journal of Computational Science*, 10,
383 77-85, <https://doi.org/10.1016/j.jocs.2014.10.004>, 2015.

384 Merz, B., Blöschl, G., Vorogushyn, S., Dottori, F., Aerts, J. C., Bates, P., Bertola, M., Kemter, M., Kreibich,
385 H., Lall, U., and Macdonald, E.: Causes, impacts and patterns of disastrous river floods. *Nature*
386 *Reviews Earth & Environment*, 2(9), 592-609, <https://doi.org/10.1038/s43017-021-00195-3>, 2021.

387 Ming, X., Liang, Q., Xia, X., Li, D., and Fowler, H. J.: Real-time flood forecasting based on a

388 high-performance 2-D hydrodynamic model and numerical weather predictions. *Water Resources*
389 *Research*, 56(7), e2019WR025583, <https://doi.org/10.1029/2019WR025583>, 2020.

390 Mori, K., Tada, K., Tawara, Y., Ohno, K., Asami, M., Kosaka, K., and Tosaka, H.: Integrated watershed
391 modeling for simulation of spatiotemporal redistribution of post-fallout radionuclides: application in
392 radiocesium fate and transport processes derived from the Fukushima accidents. *Environmental*
393 *Modelling & Software*, 72, 126-146, <https://doi.org/10.1016/j.envsoft.2015.06.012>, 2015.

394 Najibi, N., and Devineni, N.: Recent trends in the frequency and duration of global floods. *Earth System*
395 *Dynamics*, 9(2), 757-783, <https://doi.org/10.5194/esd-9-757-2018>, 2018.

396 Nanditha, J. S., Kushwaha, A. P., Singh, R., Malik, I., Solanki, H., Chuphal, D. S., Dangar, S., Mahto, S. S.,
397 Vegad, U., and Mishra, V.: The Pakistan flood of August 2022: Causes and implications. *Earth's Future*,
398 11(3), e2022EF003230, <https://doi.org/10.1029/2022EF003230>, 2023.

399 Petersen-Overleir, A.: Modelling looped rating curves. In *Proc., XXIV Nordic Hydrological Conf*, pp.
400 139-146, <https://doi.org/10.13140/2.1.1069.4403>, 2006.

401 Ruidas, D., Saha, A., Islam, A. R. M. T., Costache, R., and Pal, S. C.: Development of geo-environmental
402 factors controlled flash flood hazard map for emergency relief operation in complex hydro-geomorphic
403 environment of tropical river, India. *Environmental Science and Pollution Research*, 30, 106951-106966,
404 <https://doi.org/10.1007/s11356-022-23441-7>, 2022.

405 Sanders, B. F., Schubert, J. E., and Detwiler, R. L.: ParBreZo: A parallel, unstructured grid, Godunov-type,
406 shallow-water code for high-resolution flood inundation modeling at the regional scale. *Advances in*
407 *Water Resources*, 33(12), 1456-1467, <https://doi.org/10.1016/j.advwatres.2010.07.007>, 2010.

408 Sugawara, M.: The development of hydrological model-tank. *Time and the River: essays by eminent*
409 *hydrologists.*, 201-258, 1995.

410 Tellman, B., Sullivan, J.A., Kuhn, C., Kettner, A. J., Doyle, C. S., Brakenridge, G. R., Erickson, T. A., and
411 Slayback, D. A.: Satellite imaging reveals increased proportion of population exposed to floods. *Nature*,
412 596, 80-86, <https://doi.org/10.1038/s41586-021-03695-w>, 2021.

413 Tradowsky, J. S., Philip, S. Y., Kreienkamp, F., Kew, S. F., Lorenz, P., Arrighi, J., ... and Wanders, N.:
414 Attribution of the heavy rainfall events leading to severe flooding in Western Europe during July 2021.
415 *Climatic Change*, 176(7), 90, <https://doi.org/10.1007/s10584-023-03502-7>, 2023.

416 Valente, M., Zanellati, M., Facci, G., Zanna, N., Petrone, E., Moretti, E., Barone-Adesi, F., and Ragazzoni, L.:
417 Health system response to the 2023 floods in Emilia-Romagna, Italy: a field report. *Prehospital and*
418 *Disaster Medicine*, 38(6), 813-817, <https://doi.org/10.1017/S1049023X23006404>, 2023.

419 Ward, P. J., Jongman, B., Kumm, M., Dettinger, M. D., Sperna Weiland, F. C., and Winsemius, H. C.:
420 Strong influence of El Niño Southern Oscillation on flood risk around the world. *Proceedings of the*
421 *National Academy of Sciences*, 111(44), 15659-15664, <https://doi.org/10.1073/pnas.1409822111>, 2014.

422 Wu, H., Chen, B., Ye, X. et al.: An improved calibration and uncertainty analysis approach using a
423 multicriteria sequential algorithm for hydrological modeling. *Scientific Reports*, 11, 16954,
424 <https://doi.org/10.1038/s41598-021-96250-6>, 2021.

425 Zhu, Y. L., Ishikawa, T., Subramanian, S.S., and Luo, B.: Simultaneous analysis of slope instabilities on a
426 small catchment-scale using coupled surface and subsurface flows. *Engineering Geology*, 275, 105750,
427 <https://doi.org/10.1016/j.enggeo.2020.105750>, 2020.

428 Zhu, Y. L., Zhang, Y. F., Yang, J., Nguyen, B. T., and Wang, Y.: A novel method for calculating distributed
429 water depth and flow velocity of stormwater runoff during the heavy rainfall events. *Journal of*
430 *Hydrology*, 612, 128064, <https://doi.org/10.1016/j.jhydrol.2022.128064>, 2022.